PHYSICAL REVIEW D, VOLUME 65, 084016

# Nonlinear harmonic generation in finite amplitude black hole oscillations

Philippos Papadopoulos
*School of Computer Science and Mathematics, University of Portsmouth, Portsmouth, PO1 2EG, United Kingdom*

(Received 18 April 2001; published 27 March 2002)

The nonlinear generation of harmonics in gravitational perturbations of black holes is explored using numerical relativity based on an ingoing light-cone framework. Localized, finite, perturbations of an isolated black hole are parametrized by amplitude and angular harmonic form. The response of the black hole spacetime is monitored and its harmonic content analyzed to identify the strength of the nonlinear generation of harmonics as a function of the initial data amplitude. It is found that overwhelmingly the black hole responds at the harmonic mode perturbed, even for spacetimes with 10% of the black hole mass radiated. The coefficients for down and up scattering in harmonic space are computed for a range of couplings. Down scattering, leading to smoothing out of angular structure, is found to be equally as or more efficient than the up scatterings that would lead to increased rippling. The details of this nonlinear balance may form the quantitative mechanism by which black holes avoid fission even for arbitrary strong distortions.

DOI: 10.1103/PhysRevD.65.084016 PACS number(s): 04.30.Db, 04.70.−s

## I. INTRODUCTION

The dynamical behavior of black holes near equilibrium has been clarified using linearized perturbation theory (see, e.g., [1]). In recent years there has been interest in studying more general aspects of the dynamics of black holes as they would manifest, e.g., in the merger of two black holes [2], or in other large deformations induced by an external agent. In this regime there are no readily available analytic tools and modern approaches involve the use of numerical procedures. The most explored computational framework for the study of black hole dynamics [3] is facing a number of obstacles that limit the duration and accuracy of black hole simulations. Irrespective of the difficulties, persistent work within this approach in the past decade [4–6] has uncovered important aspects of the finite amplitude dynamics of black holes. A central conclusion of this effort has been that, in a larger than expected part of the parameter space, the physics of finite perturbations of black holes can be expressed in the language of linear perturbation analysis. It will be useful for what follows to review the main elements of this language. Linearized black hole perturbations are mapped into a problem of scattering off a positive potential which results from a combination of the angular momentum barrier with the one-way absorbing membrane of the horizon. An important role in the physics of the perturbative regime is played by the exponentially damped oscillating modes, the so-called quasinormal modes (QNM’s). Those solutions form the mechanism by which *weak* perturbations of a black hole are radiated away, leading to a stationary remnant [7].

The discovery in [4–6] that finite perturbations of black holes, seen in either black-hole–black-hole or black-hole–gravitational-wave systems, seem to emit their energy primarily through a linear channel was subsequently illuminated further with the interpretation of the numerically generated black hole spacetimes from the point of view of perturbation theory [8,9]. There have been a number of more general studies [10,11] investigating the validity of the basic picture for rotating and three-dimensional perturbations of black holes. This pioneering numerical work helped sharpen a number of questions surrounding nonlinear black hole dynamics. Is there a genuinely nonlinear regime? Is it visible to remote observers? What are the salient features of the evolution of an arbitrarily distorted black hole? Most intriguingly, how exactly does the nonlinear evolution of a highly distorted black hole avoid the perils of fission and hence conform to the area theorem expectation [12]?

The present work aims to tackle those questions by approaching the problem from a different angle, namely, by using a geometric approach based on the characteristic initial value problem (CIVP). The CIVP was introduced in seminal work by Bondi and co-workers and by Sachs [13,14] as an asymptotic, but nonperturbative, analysis of radiating spacetimes. Several variations have been proposed (see, e.g., [15–17]) to enable global computations of general spacetimes. Those formulations typically share an excellent economy and adaptability to computations of quasispherical radiative spacetimes. Versions of the CIVP have been extensively used for the study of black hole dynamics in spherical symmetry, in particular in connection with matter fields (see, e.g., [18–20]). Higher dimensional studies based on the CIVP have been rapidly maturing over the past decade. An easily accessible review is given in [21].

The work presented here is based on the framework given in [15]. The first adaptation of this formulation to the study of black holes using ingoing light-cone foliations was presented in [22], in a spherically symmetric setting. Subsequent developments led to long term stable three-dimensional computations of black holes [23]. In this paper, an algorithm developed originally for the study of regular axisymmetric spacetimes [24,25] is adapted and applied to the study of finite amplitude black hole perturbations. The approach is described in Sec. II. Special emphasis is placed on the new elements that adapt the method to the problem at hand. These include, first, initial and boundary conditions and, secondly, a method for extracting the relevant physical information. Given the substantially different nature of solutions explored here compared to the tests in [24], recalibrations and accuracy tests have been performed and pointed out where needed. In Sec. III a parameter space survey covering initial data amplitude and a portion of the harmonic space is presented. The discussion begins with the study of selected waveforms and leads to the main topic, which is the quantification of energy transfered by various nonlinear couplings. The relevance of the findings to the questions that motivated this work is assessed in the conclusions Sec. IV.

The usual unit conventions $(G=c=1)$ apply. The spacetime signature has been modified from timelike [24] to spacelike.

## II. GEOMETRIC AND COMPUTATIONAL SETUP

### A. Framework

The algorithm is based upon the CIVP for the Einstein equations in vacuum, using light cones emanating from a timelike world tube $\mathcal{W}$. With the conventions of the Bondi-Sachs gauge, the explicit form of the metric element is

$$ds^2=-\left[\left(1-\frac{2M}{r}\right)e^{2\beta}-U^2r^2e^{2\gamma}\right]dv^2+2e^{2\beta}dv\,dr$$
$$+2Ur^2e^{2\gamma}dv\,d\theta+r^2(e^{2\gamma}d\theta^2+e^{-2\gamma}\sin^2\theta\,d\phi^2). \tag{1}$$

This form implies an axisymmetric spacetime with zero rotation. The metric variables $(\gamma,M,\beta,U)$ are functions of the coordinates $(v,r,\theta)$ only. The formulation of a boundary initial value problem follows the lines of [15], with light cones emanating from the world tube $\mathcal{W}$ at a finite radius and proceeding inward, to intercept the black hole horizon (see Fig. 1). This setup may be considered as a generalization of the well known family of ingoing Eddington-Finkelstein coordinate systems to axisymmetric distorted black holes.

First we describe the overall form of the initial value problem, while the detailed equations are presented below. With the above choice of metric, the vacuum Einstein equations decompose into three hypersurface equations and one evolution equation (a further set of conservation equations along the world tube will not be used and are omitted here):

$$\Box^{(2)}\psi=\mathcal{H}_\gamma(M,\beta,U,\gamma), \tag{2}$$

$$\beta_{,r}=\mathcal{H}_\beta(\gamma), \tag{3}$$

$$U_{,rr}=\mathcal{H}_U(\beta,\gamma,U), \tag{4}$$

$$M_{,r}=\mathcal{H}_M(U,\beta,\gamma), \tag{5}$$

where $\Box^{(2)}$ is an appropriate two-dimensional wave operator acting on the $(v,r)$ submanifold, $\psi=r\gamma$, and the symbols $H_X$ denote right-hand-side contributions. Free initial data for $\gamma$ on an ingoing light cone $\mathcal{N}$ lead, with the integration of the radial hypersurface equations (3),(4),(5), to the complete metric along $\mathcal{N}$. This enables the computation of $\gamma$ on the next light cone, with the use of the evolution equation (2). This system of equations is extremely economical, given that it encodes the full content of the Einstein equations for the assumed symmetry.

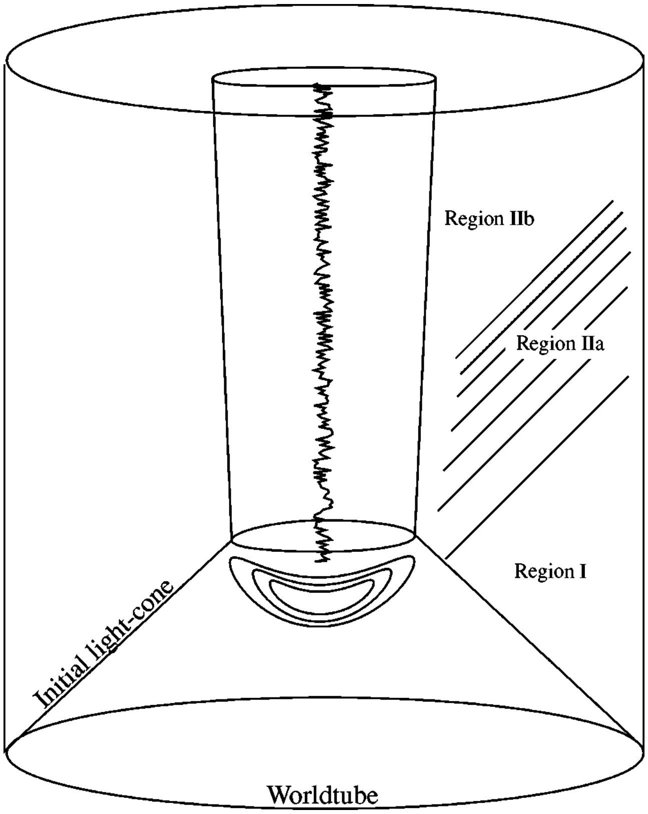

FIG. 1. Spacetime diagram illustrating the main aspects of the geometric and computational setup of the problem. The foliation is based on advanced time, using ingoing light cones that emanate from a world tube. The geometry at the world tube is kept fixed at all times and is given by the Schwarzschild values. The initial ingoing light cone is distorted with the specification of an arbitrary amount of shear. The sole constraint comes from the requirement that the ingoing light cone will not develop a caustic before one reaches a marginally trapped surface. The evolution generates a dynamic spacetime, with the initial data scattering both toward and away from the black hole. For initial data that are restricted to zero outside some given radius, there is clean propagation into the unperturbed region I, where the spacetime is Schwarzschild. The outgoing gravitational disturbance (region IIa) can be intercepted by an "observer" at a suitable radius and analyzed with respect to structure. At late times, of the order of hundreds of $M$, a slowly evolving "remnant" appears in the inner region IIb. The portion of the spacetime that emerges there represents a *distorted* black hole, the agent of distortion being the outward propagating gravitational radiation energy that intervenes between the horizon and the spherical world tube.

### B. Implementation

The computational algorithm follows closely that developed in [24] and differs only in the boundary treatment and in the sense in which the integration proceeds (here toward smaller radii). The algorithm was shown to be second order accurate in the nonlinear regime using a static boost-symmetric solution (SIMPLE) and in the linear regime using exact decaying multipole solutions for harmonics up to $l=6$. In addition the consistency of the evolution was checked using global energy conservation. Here we briefly review the methodology in order to facilitate the presentation of the new numerical results.

The coordinate system consists of a radial $r$ coordinate and an angular $y=-\cos\theta$ coordinate. The numerical grid is uniformly spaced in both. In the following expressions $\theta$ is understood to stand for $\cos^{-1}y$. We use the normalized variables $\hat{U}=U/\sin\theta$ and $\hat{\gamma}=\gamma/\sin^2\theta$.

The hypersurface equations for the fields $\beta,\hat{U},M$ are given by

$$\beta_{,r}=\frac{1}{2}r\sin^4\theta(\hat{\gamma}_{,r})^2, \tag{6}$$

$$\begin{aligned}(r^4e^{2(\gamma-\beta)}\hat{U}_{,r})_{,r}=2r^2\bigg(&\beta_{,ry}-\frac{2}{r}\beta_{,y}-\sin^2\theta\hat{\gamma}_{,ry}+4y\hat{\gamma}_{,r}\\&+2\sin^4\theta\hat{\gamma}_{,r}\hat{\gamma}_{,y}-4y\sin^2\theta\hat{\gamma}\hat{\gamma}_{,r}\bigg),\end{aligned} \tag{7}$$

$$\begin{aligned}M_{,r}=\frac{1}{2}+\frac{1}{8}&\sin^2\theta e^{2(\gamma-\beta)}(\hat{U}_{,r})^2+2ry\hat{U}\\&+\frac{1}{2}r^2y\hat{U}_{,r}-r\sin^2\theta\hat{U}_{,y}-\frac{1}{4}r^2\sin^2\theta\hat{U}_{,ry}\\&+\frac{1}{2}e^{2(\beta-\gamma)}[-1-2y\beta_{,y}+\sin^2\theta\beta_{,yy}\\&+\sin^2\theta(\beta_{,y})^2-2(5y^2-1)\hat{\gamma}\\&+8y\sin^2\theta\hat{\gamma}_{,y}-\sin^4\theta\hat{\gamma}_{,yy}+8y^2\sin^2\theta\hat{\gamma}^2\\&-8y\sin^4\theta\hat{\gamma}\hat{\gamma}_{,y}+2\sin^6\theta(\hat{\gamma}_{,y})^2\\&+4y\sin^2\theta\hat{\gamma}\beta_{,y}-2\sin^4\theta\beta_{,y}\hat{\gamma}_{,y}].\end{aligned} \tag{8}$$

The evolution equation for the field $\psi=r\hat{\gamma}$ is given by

$$\begin{aligned}e^{2\beta}\Box^{(2)}\psi=\hat{U}_{,y}+\frac{r}{2}\hat{U}_{,ry}-\frac{2}{r}\left(M_{,r}-\frac{M}{r}\right)\hat{\gamma}+\sin^2\theta(r\hat{U}_{,r}\hat{\gamma}_{,y}\\+2r\hat{U}\hat{\gamma}_{,ry}+2\hat{U}\hat{\gamma}_{,y}+r\hat{\gamma}_{,r}\hat{U}_{,y})-2y(3r\hat{\gamma}_{,r}\hat{U}\\+2\hat{U}\hat{\gamma}+r\hat{U}_{,r}\hat{\gamma})-\frac{1}{4}r^3(\hat{U}_{,r})^2e^{2(\gamma-\beta)}\\-\frac{1}{r}(\beta_{,y}^2+\beta_{,yy})e^{2(\beta-\gamma)},\end{aligned} \tag{9}$$

where

$$\Box^{(2)}\psi=e^{-2\beta}\left[2\hat{\psi}_{,vr}+\left(\frac{V}{r}\hat{\psi}_{,r}\right)_{,r}\right]. \tag{10}$$

We briefly review the elements of the numerical integration procedure. The hypersurface equations are discretized directly using centered differences and integrated inward as ordinary differential equations. The discretization of the evolution equation follows the so called ‘‘null parallelogram’’ procedure (see Fig. 2). The two dimensional wave operator (10) is integrated over the $(v,r)$ parallelogram spanned by the ingoing light cones $v^n$ and $v^{n+1}$ and the outgoing null geodesic segments $AB$ and $DC$. The resulting integral relates the field values $\psi_A,\psi_B,\psi_C,\psi_D$ to the value of $\mathcal{H}_\gamma$ at the center of the parallelogram. This allows us to obtain a marching algorithm which, starting from zero data for $\psi$ at the world tube $\mathcal{W}$, provides the evolution of the field in the entire interior of the world tube. Inside the trapped region the ‘‘outgoing’’ characteristics are also pointing inwards (segment $EF$ in Fig. 2). This does not prohibit the application of the parallelogram rule. What *is* different inside the horizon is that we can stop the integration at any radius, without requiring any boundary condition (excision).

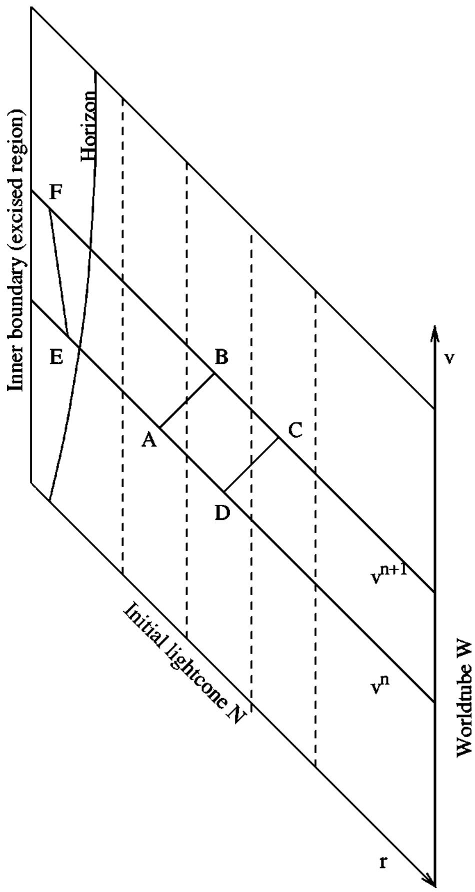

FIG. 2. Diagram illustrating the structure of the integration procedure. Depicted is the spacetime grid for *one particular angle*. Initial data are set on the initial null cone $\mathcal{N}$. Boundary conditions $(M=M_0)$ are set on the world tube $\mathcal{W}$. Successive levels of advanced time $v$ are depicted (diagonal lines $v^n,v^{n+1}$) along with the radial grid (dashed vertical lines). The radial grid starts at the world tube $\mathcal{W}$ and terminates inside the horizon. The evolution equation for $\gamma$ relates the field values $\psi_A,\psi_B,\psi_C,\psi_D$ to the value of $\mathcal{H}_\gamma$ at the center of the parallelogram. This allows one to obtain a marching algorithm which, starting from zero data for $\psi$ at the world tube $\mathcal{W}$, gives the evolution of the field in the entire interior of the world tube.

The numerical evolution is formulated in an explicit manner, and is hence subject to a Courant-Friedrich-Levy (CFL) stability condition. This is derived by considering the backward light cone from a grid point at $(v,r,y)$. This light-cone must be contained within the numerical "stencil" used for the integration procedure. There are two relevant constraints. By examining the radial direction $(dy=0,d\phi=0)$ it can be seen immediately from the line element that the constraint is

$$\left(1-\frac{2M}{r}-U^2r^2e^{2(\gamma-\beta)}\right)dv\leq 2\,dr. \tag{11}$$

Similarly, for the increasing/decreasing angular directions $(dr=0,d\phi=0)$ one obtains the constraints

$$\left(e^{\beta-\gamma}\sqrt{1-\frac{2M}{r}}\pm U\right)dv\leq r\,dy/\sqrt{(}1-y^2). \tag{12}$$

For a convergent and stable evolution at each time step we search for the smallest $dv$ dictated by the metric variables as the evolution proceeds. In practice, for the evolutions presented here the time step was always costrained by the radial condition (11). It is worth noting that in the black hole case under consideration the origin of the coordinate system is not the vertex of a light cone, and the constraint imposed by the CFL condition is much weaker than the one found in [24]. In fact the computational cost and accuracy of those fully nonlinear simulations are comparable to those of axisymmetric (2+1) calculations based on linearized theory [28].

The black hole dynamics problem is sufficiently different and computationally challenging [27] though that a recalibration of the code has been performed. High resolution calculations involve 2000 radial grid points covering the radial domain from $r_{\min}=1.8M$ to $r_{\max}=60M$. This corresponds to $\Delta r=0.03M$. An angular resolution of 90 grid points covering the angular domain $y=[-1,1]$ corresponds to $\Delta\theta=0.02$ at the equator and $\Delta\theta=0.1$ at the pole, i.e., the grid is uniform in the $y$ coordinate, but not uniform in $\theta$. A visual representation of the coverage of the ingoing light cones by grid points is given in Fig. 3. For the assessment of the accuracy of the results, evolutions using a second grid, with half the resolution (i.e., $1000\times45$) in both directions, will be used throughout. It was found that, for the high resolution grid, the primary harmonic can safely be captured to better than 1%. The good accuracy of the code does not automatically guarantee the correct capturing of the nonlinear effects, as those are features developed during the evolution, and hence potentially requiring additional resolution. For this reason, quantitative statements about such effects will be individually certified as will be shown below. Evolution for a total time of $120M$ requires about 30 min of a 666 MHz Alpha CPU, at roughly 240 megaflops. About 45% of that time is spend on the update of the dynamical variable $\gamma$, with the rest being distributed among the hypersurface integrations and auxiliary tasks.

### C. Boundary and initial data

Within an ingoing light-cone framework, there are two possible prescriptions for setting up initial and boundary data for the study of the response of a black hole to perturbations. In the first, akin to a *scattering* study, the initial advanced time light cone $\mathcal{N}$ has trivial background data. Incoming gravitational radiation is introduced at the world tube $\mathcal{W}$ through the specification of the unconstrained $\gamma(v,y)|_{\mathcal{W}}$ function. A self-consistent evolution of the boundary data is then achieved by the time integration of the conservation conditions along the world tube. In the second approach, which may be called a *perturbation* study, the free data are specified on $\mathcal{N}$, whereas $\mathcal{W}$ is kept with trivial data. The two approaches are closely linked, since the scattering of incoming radiation will immediately lead to outgoing perturbations. Still, the perturbation approach is computationally simpler, since it avoids the integration of the conservation conditions. This is the approach used here.

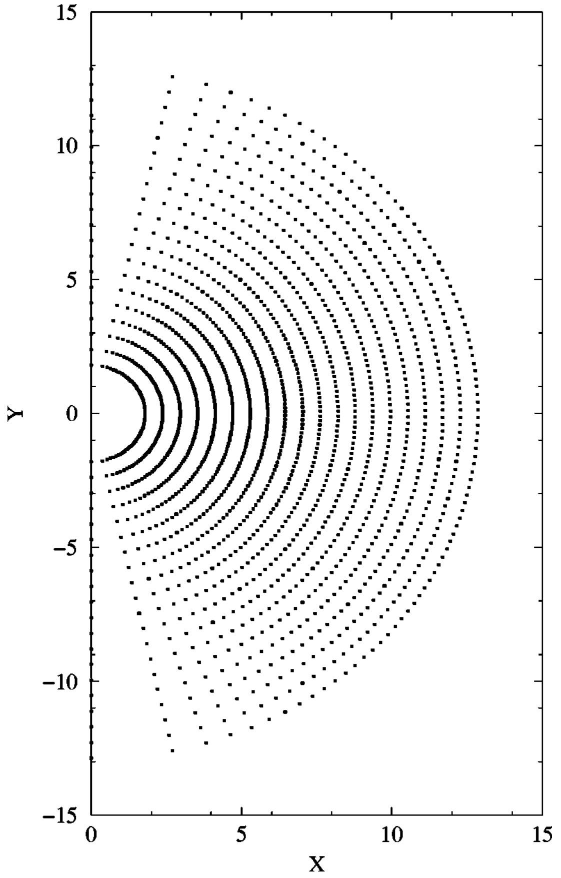

FIG. 3. Illustration of the distribution of grid points on the ingoing light cone using a pseudo-Cartesian space ($X=r\cos\theta,Y=r\sin\theta$). The points $X=0$ denote the axis of symmetry, whereas $Y=0$ denotes the equatorial plane. The uniform radial spacing is visible. We note that the figure depicts the actual high resolution grid points $(2000\times90)$, except that only the innermost fifth of the radial extent of the grid is shown and only every tenth radial point is shown. The innermost radius is chosen to lie inside the horizon and subsequent evolution can only make the horizon grow. The entire set of angular directions is shown. The uniform spacing in the $y=-\cos\theta$ coordinate is translated into a non uniform grid in the $\theta$ coordinate. The $y$ coordinate is optimally adapted to capturing the Legendre polynomial type dependence of radiative fields.

The world tube boundary conditions are simple but central to the setup of the physical problem. A nonrotating unit-mass black hole is prescribed at $\mathcal{W}$ by setting $M(v,r_{\mathcal{W}})=1$

and all other fields equal to zero. Such a condition is not in general compatible with a spacetime in which outgoing radiation is filtering through the world tube. Minimally, such radiation would be diminishing the mass contained inside the world tube, and $M(v,r_{\mathcal{W}})$ would not be constant. Hence, for consistency, evolutions must be restricted in time so that the neighborhood of the world tube is unperturbed by the local flux of radiation. Satisfying this condition is entirely possible and will always be the case in the results presented here.

The free initial data on the ingoing light cone $\mathcal{N}$ are captured by a single real function of two variables $\gamma(r,y)$. (For a spherical unperturbed spacetime this function is identically zero.) We will choose initial data of the form $\gamma(r,y) = R(r)A(y)$. For the radial profile $R(r)$ we adopt an exponentially decaying profile $e^{-(r-r_c)^2/\sigma^2}$, as a model of a localized disturbance superposed on a black hole. Evolution with different values for $r_c$ suggests that values close to $r=3M$ are more effective in generating outgoing nonlinear response and this value will be adopted throughout.

The *angular profile* $A(y)$ of the initial data and their evolution will play a key role in the following discussion because it is the primary means by which we can identify the action of nonlinear mechanisms. The only constraint is that the function has suitable behavior at the pole $y=\pm 1$, consistent with the fact that $\gamma$ is a spin-2 scalar representing the everywhere regular intrinsic metric of topological spheres of constant $r$. This regularity condition is equivalent to requiring that the angular decomposition of $\gamma$ in harmonics starts with at least a quadrupole term. The spin harmonics relevant to this decomposition are discussed in detail in [26]. In axisymmetry, a convenient expression for the basis functions is given by

$$Y_{2l0} = \left( \frac{(l-2)!(2l+1)}{4\pi(l+2)!} \right)^{1/2} (1-y^2) P_{l,yy}, \tag{13}$$

where $Y_{2lm}$ denotes an $(l,m)$ harmonic of spin 2 and $P_l$ are the Legendre polynomials.

In summary then, the initial data on the ingoing light cone $\mathcal{N}$ are given by the expression

$$\gamma(r,y) = \frac{\lambda}{\sqrt{2\pi}\sigma} e^{-(r-r_c)^2/\sigma^2} Y_{2l0}(y). \tag{14}$$

The multipole index $l$ of the initial data will be referred to as the *primary harmonic*, as it is to be expected that it will play an important role in the response of the black hole geometry to the perturbations. The physical content of such data is essentially a local distortion of the ingoing light cone, with prescribed angular structure and amplitude.

Some clarifications are worthwhile here. Although one can imagine situations that lead to initial data qualitatively different from the above expression, our experience with the evolution of various types of data show that the response of the black hole to data of compact support around the horizon always follows the same pattern. The claim that the spacetime constructed by this approach is actually a distorted black hole is made geometrically more precise by the introduction of the concept of a marginally trapped two-surface (MTS) on a given ingoing light cone $\mathcal{N}$. A MTS is defined, in this context, as the two-parameter radial function $R(r,y)$ on which the expansion $\Theta = 2\nabla^{\alpha} l_{\alpha}$ of an outgoing null ray pencil $l^{\alpha}$ vanishes [22]. Using a relaxation method for the solution of the equation $\Theta=0$ one obtains indeed a distorted initial MTS, showing curvature dependent on the amplitude of the data. The invariant analysis of the intrinsic geometry and dynamics of the MTS are interesting problems in themselves and deserve separate study.

### D. Extraction of the nonlinear response

The evolution of the initial data leads, in general, to radiation emission toward both infinity and the horizon. In Fig. 4 we show typical snapshots of such evolutions. Here the focus will be on the outgoing, in principle observable, part. The nonlinear response of the black hole to the initial perturbation will be encoded quite legibly in the angular harmonic decomposition of the outgoing solution. A strategy to isolate this information is outlined here.

The metric perturbation encoded in $\gamma$ can be decomposed in spin-2 harmonics as

$$\gamma(v,r,y) = \sum_{l=2}^{\infty} \gamma_l(v,r) Y_{2l0}(y), \tag{15}$$

which is inverted as

$$\gamma_l(v,r) = 2\pi \int_{-1}^{1} \gamma(v,r,y) Y_{2l0}(y) dy, \tag{16}$$

using the orthonormality of the spin-2 harmonics. At this stage the decomposition is nonperturbative, i.e., it does not depend on $\gamma$ being small and can be carried out across the entire light cone. The set of functions $\gamma_l(v,r)$ effectively captures all the information about the given spacetime. For nonlinear evolutions, this set includes more than one harmonic, even if the initial data are set to a single (the primary) harmonic dependence. The new harmonics will be referred to as the *secondary harmonics*. In numerical practice, this decomposition is obtained via an eighth-order accurate (in $\Delta y$) angular integration of the grid data.

A good indicator of nonlinear processes near the black hole is the amount of energy emitted in secondary harmonics. In the present setup the foliation does not extend to infinity; hence the extraction of an energy estimate for an outgoing solution must resort to an approximate expression. The task is straightforward, due to the form of the metric element adopted (i.e., spherical coordinates, light-cone gauge). Further, sufficiently far from the black hole (but inside the world tube), the outgoing radiation is weak in amplitude and the spacetime is close to a Schwarzschild spacetime in its standard ingoing Eddington-Finkelstein form. At that radius, denoted as the observer radius $r_o$, and forming a timelike world tube of area $4\pi r_o^2$, the *news* can be approximated by $c(v) = \psi(v) = r_o \gamma(v)$. From this, it follows that the total (negative) energy flux crossing the observer will approximate Bondi's energy flux integral

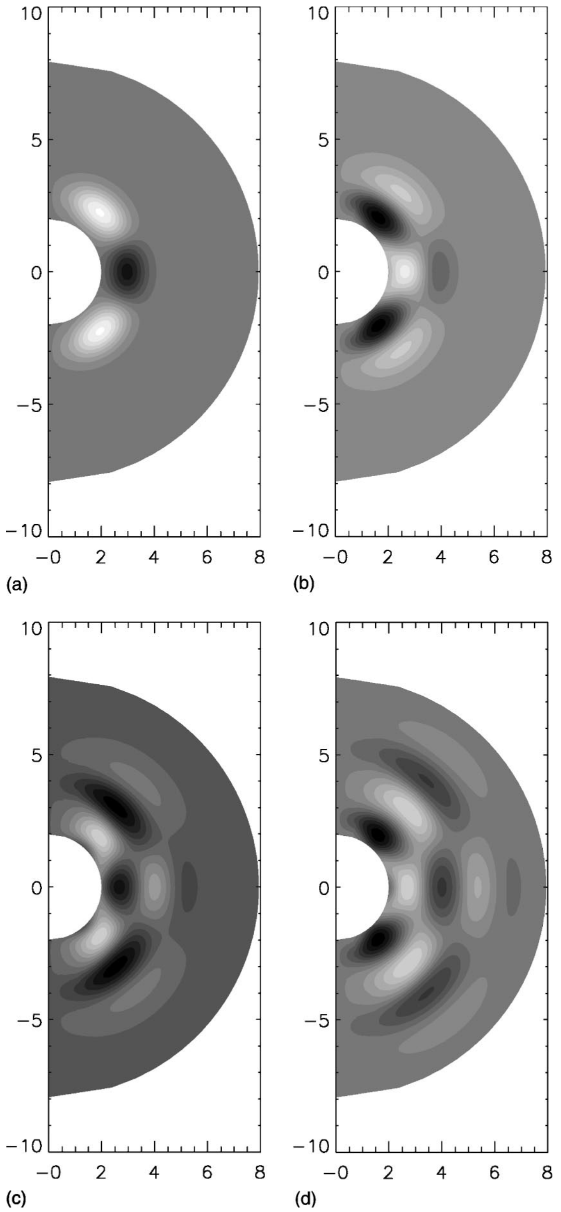

FIG. 4. Sequence of snapshots illustrating the evolution of finite amplitude black hole oscillations via an ingoing light-cone approach. The upper left panel shows the initial data (field $\phi = r\gamma$), representing a localized finite amplitude perturbation of a black hole. The plot coordinates are pseudo-Cartesian $X = r\cos\theta, Y = r\sin\theta$, hence placing the axis of symmetry along $X=0$ and the equator along $Y=0$. Shown are contour levels of the distortion of the light cone (white denotes large positive values while black denotes large negative values). In this case the initial datum is an $l=4$ harmonic. The next snapshot (upper right panel) shows the evolution of $\psi$ at $v=2.47M$. The outward propagation of the data is visible but also the change of phase near the horizon. The sequence proceeds with the lower left panel, at time $v=6.18$. By this time one further node is visible in the radial profile. The evolution continues in the lower right panel ($v=9.89$), where three nodes are visible. The panels show only the innermost regions of the computational domain (about 1/20 of the total radial extent). Despite the oscillatory nature of these first cycles, examination of the signal shows that only for later oscillations does the black hole spacetime approach the typical quasinormal-mode ringing.

$$\frac{dE_{tot}}{dv} = -\frac{1}{4\pi}\oint (\psi_{,v})^2 dy\, d\phi. \tag{17}$$

An expression for the total energy emitted in each angular mode $l$ after evolution to a final time $T$ is given by

$$E_l(T) = \frac{1}{4\pi} r_o^2 \int_0^T (\gamma_{l,v})^2 dv. \tag{18}$$

Given the availability of the complete spacetime, the device developed here is but a partial probe whose usefulness rests on its quantitative nature.

Other nonlinear effects will include, for example, deviations of the oscillation frequencies from the weak field limit. Those effects need careful differentiation from the natural inclusion of higher overtones, which are present in the initial response of linearized perturbations as well. They also appear, at first sight, difficult to quantify and for this reason will play a lesser role in this study.

## III. NONLINEAR EVOLUTION RESULTS

It is appropriate to start with the venerable quadrupole perturbation [$l=2$ in Eq. (14)], and fix $\sigma=0.5, r_c=3.0$. This introduces a finite perturbation positioned squarely on the potential barrier of classic perturbation theory. The various runs (the complete list is given in Table I) are parametrized by the amplitude of the initial data, $\lambda$. The range of amplitudes explored is defined on the one end by the requirement that nonlinear effects are stronger than numerical truncation error and on the other by the necessity that the evolution maintains a smooth, well behaved, ingoing light-cone foliation. For sufficiently strong data the geometry is seen to develop kinks, along specific angles, starting first at the innermost radial points (one can always hasten the end of the foliation by evolving deeper inside the horizon). For evolutions just below the breakdown amplitude, those features require increasingly larger angular resolution to resolve. The strong field effects responsible for the caustic formation at the inner edges of the domain have not been found to be reflected in the actual observed nonlinear behavior. For this reason the results presented here do not attempt to capture the precise limits of the caustic-free regime.

Illustrated here is the strongest case, $\lambda=0.25$. The response of the black hole to this perturbation is shown in Fig. 5, as registered by an observer located at $20M$. The arrival time of the primary response is roughly twice the radial separation of the observer from the black hole ($40M$), reflecting the fact that outgoing light waves propagate at coordinate speed 1/2 in an ingoing light-cone framework. The primary (quadrupole) response carries, for this amplitude, almost 10% of the black hole mass in radiation. An $l=2$ perturbation carries no linear momentum (it is reflection symmetric with respect to the equator) and hence one does not expect to see an output of odd harmonics. Given the large amount of radiated energy, one would expect that the couplings in the right-hand side of the evolution equation (2) will generate some even-harmonic signal. In this case, given that the primary is the lowest allowed harmonic, all secondary re-

TABLE I. Cumulative data for energy transfer between harmonic modes in nonlinear black hole perturbations. The left column shows the type of initial distortion (harmonic index and amplitude). The highest amplitude in each $l$ family corresponds roughly to the strongest data that will evolve without forming a caustic near the horizon. For $l=2$ and $l=3$ the energy carried by such data is about 10% of the black hole mass. For $l=4$ it is an order of magnitude less. The off-diagonal elements of the table tell the story of secondary harmonic generation, toward smoothing or rippling the primary. They have a variety of scalings and coupling strengths, which are captured better in the graph of Fig. 4. The zero values in the entries denote round off generated measurements that are typically less than $10^{-20}$. Error estimates are based on results from lower resolution runs. Error values below 1% have been rounded up to that value.

| Input data | | Output energy in harmonics (in units of $M$) | | | | |
|---|---|---|---|---|---|---|
| $l$ | $\lambda$ | $E_2$ | $E_3$ | $E_4$ | $E_5$ | $E_6$ |
| 2 | 0.25 | $(0.97\pm0.01)\times10^{-1}$ | 0 | $(0.41\pm0.01)\times10^{-2}$ | 0 | $(0.42\pm0.04)\times10^{-3}$ |
| | 0.177 | $(0.45\pm0.01)\times10^{-1}$ | 0 | $(0.98\pm0.01)\times10^{-3}$ | 0 | $(0.47\pm0.02)\times10^{-4}$ |
| | 0.125 | $(0.21\pm0.01)\times10^{-1}$ | 0 | $(0.23\pm0.01)\times10^{-3}$ | 0 | $(0.52\pm0.01)\times10^{-5}$ |
| | 0.0884 | $(0.10\pm0.01)\times10^{-1}$ | 0 | $(0.54\pm0.01)\times10^{-4}$ | 0 | $(0.60\pm0.01)\times10^{-6}$ |
| | 0.0625 | $(0.51\pm0.01)\times10^{-2}$ | 0 | $(0.13\pm0.01)\times10^{-4}$ | 0 | $(0.71\pm0.01)\times10^{-7}$ |
| 3 | 0.25 | $(0.87\pm0.05)\times10^{-4}$ | $(0.11\pm0.01)\times10^{-1}$ | $(0.23\pm0.01)\times10^{-4}$ | $(0.36\pm0.01)\times10^{-6}$ | $(0.87\pm0.02)\times10^{-4}$ |
| | 0.177 | $(0.19\pm0.01)\times10^{-4}$ | $(0.54\pm0.01)\times10^{-2}$ | $(0.57\pm0.03)\times10^{-5}$ | $(0.45\pm0.01)\times10^{-7}$ | $(0.22\pm0.01)\times10^{-4}$ |
| | 0.125 | $(0.47\pm0.03)\times10^{-5}$ | $(0.27\pm0.01)\times10^{-2}$ | $(0.14\pm0.01)\times10^{-5}$ | $(0.55\pm0.01)\times10^{-8}$ | $(0.53\pm0.01)\times10^{-5}$ |
| | 0.0884 | $(0.12\pm0.01)\times10^{-5}$ | $(0.14\pm0.01)\times10^{-2}$ | $(0.35\pm0.02)\times10^{-6}$ | $(0.70\pm0.01)\times10^{-9}$ | $(0.13\pm0.01)\times10^{-5}$ |
| | 0.0625 | $(0.29\pm0.02)\times10^{-6}$ | $(0.67\pm0.01)\times10^{-3}$ | $(0.89\pm0.05)\times10^{-7}$ | $(0.86\pm0.03)\times10^{-10}$ | $(0.33\pm0.01)\times10^{-6}$ |
| 4 | 0.075 | $(0.75\pm0.04)\times10^{-4}$ | 0 | $(0.86\pm0.01)\times10^{-2}$ | 0 | $(0.14\pm0.02)\times10^{-4}$ |
| | 0.053 | $(0.18\pm0.02)\times10^{-4}$ | 0 | $(0.42\pm0.01)\times10^{-2}$ | 0 | $(0.33\pm0.04)\times10^{-5}$ |
| 4 | 0.0375 | $(0.43\pm0.04)\times10^{-5}$ | 0 | $(0.20\pm0.01)\times10^{-2}$ | 0 | $(0.79\pm0.10)\times10^{-6}$ |
| | 0.0265 | $(0.10\pm0.01)\times10^{-5}$ | 0 | $(0.10\pm0.01)\times10^{-2}$ | 0 | $(0.19\pm0.02)\times10^{-6}$ |
| | 0.0187 | $(0.25\pm0.03)\times10^{-6}$ | 0 | $(0.50\pm0.01)\times10^{-3}$ | 0 | $(0.46\pm0.06)\times10^{-7}$ |

sponses will have higher $l$ values (up scattering in $l$ space) and will therefore tend to create further *ripples* in the predominantly spherical black hole geometry. A first taste of the quantitative result follows from the observed amplitudes of the secondary harmonics ($l=4,6$): They are respectively one and two orders of magnitude lower in amplitude. Odd harmonics do not appear, up to round-off error.

The typical damped oscillatory behavior known from linearized analysis is visible here also for large finite perturbations. Looking closer into the secondaries one notes that, with respect to the primary wave, the global maxima of the secondary harmonics (i) are slightly delayed and (ii) have phase reversals (i.e., the global maxima alternate in sign). Given that the primary wave has a peak at negative amplitude, the origin of the $l=4$ secondary waves in quadratic coupling may explain the phase reversal. Similarly, the cubic coupling for the $l=6$ wave may account for the second reversal seen there. This claim will be strengthened by the analysis of the functional dependence on the initial data amplitude later on. The evident time delay is harder to account for.

We proceed next to a family of runs where the initial data are set to an $l=3$ harmonic. This case differs markedly in physical content from the one described previously, as the initial data do not exhibit equatorial reflection symmetry and posses net linear momentum. In addition, the fact that the $l=3$ harmonic is not the lowest allowed oscillation mode raises the possibility that the secondary harmonics have both higher and lower angular structure. The down scattering to lower $l$ values is particularly interesting, as it represents a mechanism by which energy is lost from the primary harmonic to a smoother configuration. The response for a family of data of identical radial profile is monitored again, at the same finite radius. The five different profiles shown in Figs. 6 and 7 are the time-dependent amplitudes of the harmonically decomposed signal at the observer (harmonics $l=2$ to 6) for an amplitude of $\lambda=0.25$. The strongest signal corresponds to the multipole geometry of the initial perturbation. The present situation is in contrast to the previous example, where the equatorial reflection symmetry (zero linear momentum) of the primary mode was reflected in all secondaries. Despite the fact that the primary mode carries linear momentum, the secondaries are anything but reflection antisymmetric. In fact, the nearest anti-symmetric mode ($l=5$) is the weakest in amplitude. Whereas the damped oscillation theme is still dominant, some subtleties are more apparent here. This can be seen most easily in the large change in the periods of the $l=2$ mode between the early and late parts of the signal and also in the significant modulation seen in the $l=5$ mode.

It is not clear how to effectively characterize damped oscillating signals with brief duration and strong variability. The plots in Fig. 8 attempt at least a qualitative analysis in the following manner. For each harmonic, the zero crossing of the signal at the observer is recorded. Successive zero crossings provide an instantaneous value for the half period of the oscillation. This is plotted as a function of time, illustrating in this manner the *evolution* of the signal frequency in time. The horizontal lines in that panel are half periods for QNM oscillations of even-parity perturbations of Schwarzschild black holes [1]. The QNM periods are $T=16.81,10.48,7.76,6.21,5.18$ (in units of $M$) for perturbations of $l=2,\ldots,6$ type, respectively. The very strong (dou-

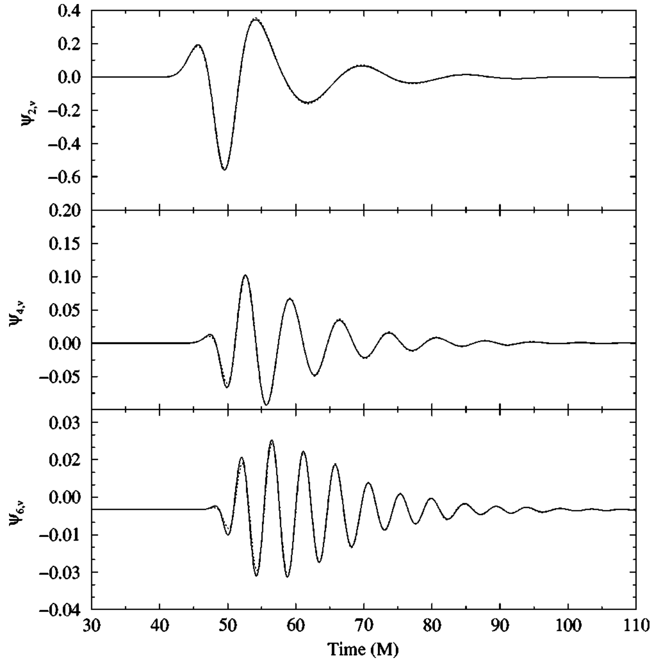

FIG. 5. Gravitational radiation signals from a black hole perturbed with quadrupole initial data. The three different panels show the time-dependent amplitudes of the harmonically decomposed signal at the observer (harmonics $l=2,4$, and 6). The top panel shows the strongest response (primary harmonic). The tail of all modes exhibits the typical damped oscillatory behavior known from linearized analysis. There are large amplitude differences between the various modes which are quantified in detail. The higher harmonics exhibit a time lag of the first peak with respect to the primary excitation. Note also the successive phase reversal in the secondary harmonics. The primary signal has a negative global maximum which becomes a positive one for $\psi_{4,v}$ and again a negative one for $\psi_{6,v}$. For the purpose of illustrating visually the code accuracy, each panel shows two lines, a solid one corresponding to the high resolution grid and a dotted one corresponding to half that resolution.

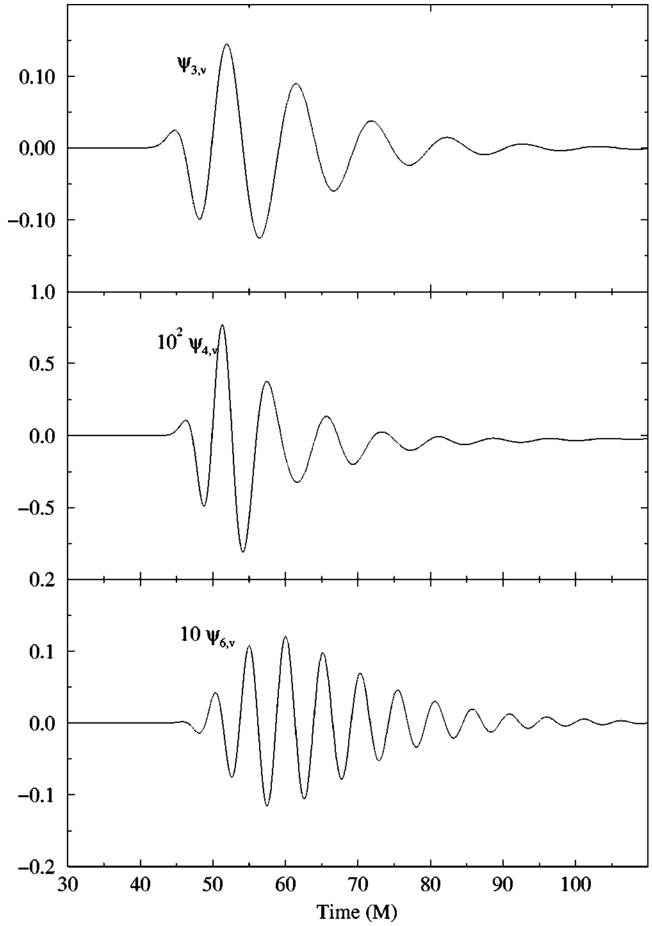

FIG. 6. Gravitational radiation signals from an $l=3$ distortion of a black hole. The three different panels show the time-dependent amplitudes of the harmonically decomposed signal (harmonics $l=3,4,6$). The top panel shows the primary harmonic ($l=3$). One notes immediately that for a primary mode with intrinsic linear momentum (odd $l$ values) *all* secondary modes are excited. Again the amplitudes of the various harmonics vary considerably (note the multiplication factors denoted in the panels). The damped oscillation picture is still recognisable in all signals, but many peculiarities are visible even on cursory inspection.

bling) of the frequency of the $l=2$ harmonic is notable. The frequency asymptotes to the weak field value, but only after substantial evolution time. The primary harmonic ($l=3$) is less strongly evolving and attains its weak field value earlier on. The $l=5$ response also exhibits the strong time evolution seen in the quadrupole and reaches its weak field value late in the evolution. The $l=4$ periods are problematic and only the few initial estimates are shown. This is despite the, at first sight, normal appearance of the signal. The reason has been traced to the secular evolution of the black hole remnant (region IIb of Fig. 1) which affects the time derivative of the field at the observer. Recall that the effective energy content between the world tube and the horizon acts tidally on the black hole and distorts it. There is a small physical amount of energy loss, as radiation is absorbed by the horizon, and possibly to numerical dissipation. Both effects would lead to a slow evolution of the remnant, which is captured by the time-dependent value of $\gamma_{,v}$ at the observer. The effect will be more pronounced for harmonics that match more closely the geometry of the remnant (here the $l=4$) and are weak in amplitude. The tail of the $l=4$ signal is seen not to asymptote to zero, but rather to a small negative value. Examining the second time derivative and/or using observers placed farther away may help reduce this effect, but frequency considerations are not central to this study and this is not pursued further. An oscillatory effect of possibly the same or similar origin affects the late time periods of the ($l=6$) harmonic which are seen to oscillate about the QNM value.

Keeping with the same setup, the evolution of an $l=4$ primary is studied. This case is physically close to the quadrupole one, except that here it is possible to have down scattering to the quadrupole harmonic. This adds new scope to the analysis, as it allows comparison of the up scattering mechanism from 2 to 4 to the down scattering from 4 to 2. One relevant difference of the $l=4$ primary is that caustics appear to be forming here for weaker data (about one-tenth the total energy of the $l=2,3$ cases). This is possibly due to more efficient focusing of ingoing rays by data of the same

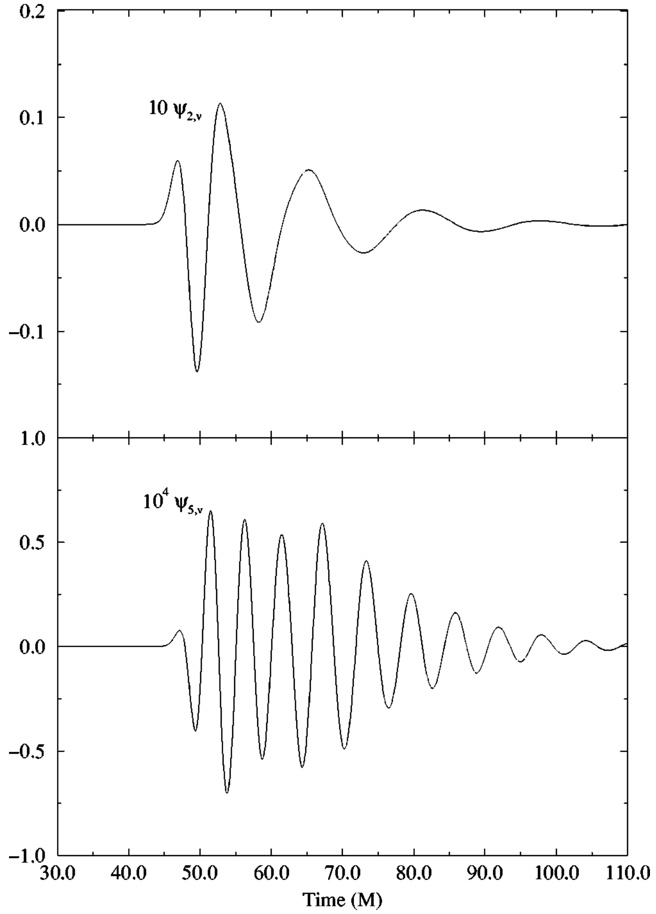

FIG. 7. Gravitational radiation signals from an $l=3$ distortion of a black hole (as Fig. 6). Here we see amplitudes of the harmonically decomposed signal for harmonics $l=2$ and $l=5$.

total energy if those data have angular structure.

The cumulative energy calculations for the three scenarios are presented in Table I. This table is the central result of this paper and hence warrants some discussion. The range of chosen amplitudes has already been justified. The range of harmonics studied is a compromise between reasonable completeness and finite resources. The error bars are important in establishing confidence in those particular numbers. They are evaluated by performing the same calculation again, with exactly twice the resolution, and taking the difference in calculated energy as a measure of confidence. Numerical effects can artificially generate or suppress harmonics, e.g., through boundary effects and dispersion. In addition, dissipation will affect the amplitudes. Low resolution is particularly dangerous for down-scattered modes, and it is found that there is a minimum angular resolution required for the nonlinear signal to rise above the truncation error. The error bars serve as a guard against attempting to resolve too subtle an effect.

For the range of data studied, the energy in any mode is always a monotonically increasing function of the initial data amplitude. There is energy in all modes, except for those couplings excluded by the conservation of linear momentum. The forbidden couplings typically show energy well below $10^{-20}$, which suggests an origin in round-off error. Indirectly this suggests that the discretized version of the equations (and its implementation) respects a conservation law as well. Almost the entire content of Table I can be grasped easily by putting the data on a log-log graph as in Fig. 9. This graph excludes the primary harmonic data (diagonal elements of the table), as those encode how much energy is *subtracted* from the mode as a function of initial data amplitude, whereas the off-diagonal terms capture how much energy is *added* to the mode. It is immediately seen that the energy versus amplitude relation is a power law for all cases, but with different slopes and normalizations that can be described by

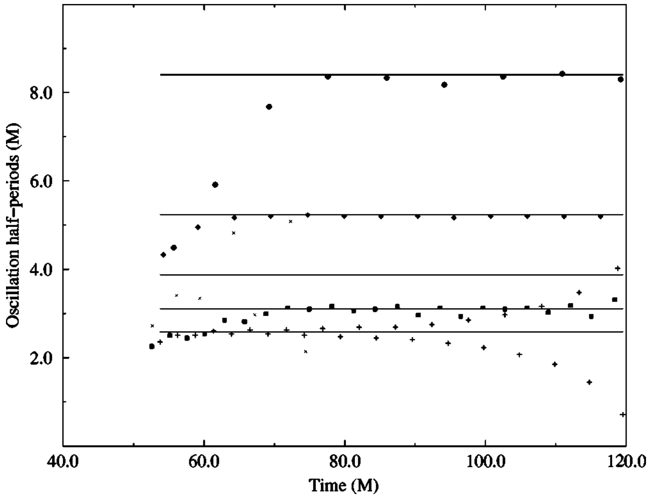

FIG. 8. Emergence of quasi-normal-ringing signals at late times. The panel illustrates a time domain analysis of the frequency content of the signals in the following fashion. Illustrated are the zero crossings of the various harmonics as a function of arrival time. Filled circles, diamonds, and squares correspond to $l=2,3,5$ respectively. Crosses denote $l=4$ and pluses denote $l=6$. The horizontal lines are half periods for QNM oscillations of even-parity perturbations of Schwarzschild black holes. There is generally good agreement, after about 30M, but substantial deviations initially. The $l=4$ case exhibits some peculiarity which is discussed in the text.

$$E_{ll'}=\epsilon_{ll'}\lambda^{s_{ll'}}M, \tag{19}$$

where the first (second) indices denote the primary (secondary) harmonics, respectively. The exponent $s_{ll'}$ will, in general, follow from the type of coupling, i.e., it reflects a geometric feature of the theory. The coupling coefficient $\epsilon_{ll'}$ captures the efficiency of the coupling, in the sense that larger coefficients indicate stronger coupling of modes. The values of the coefficients are closely associated with the detailed structure of the solution, in the region where nonlinear couplings are active. With linear best fits to the data points, one can estimate values for $(s_{ll'},\epsilon_{ll'})$ (Table II).

Upon examining the table of numerical fits it is clear that the quadratic couplings dominate the various transitions (a quadratic coupling generates a fourth-order energy scaling). There are two examples of higher couplings (cubic in the amplitude), namely, the $2\rightarrow6$ and the $3\rightarrow5$. There are sev-

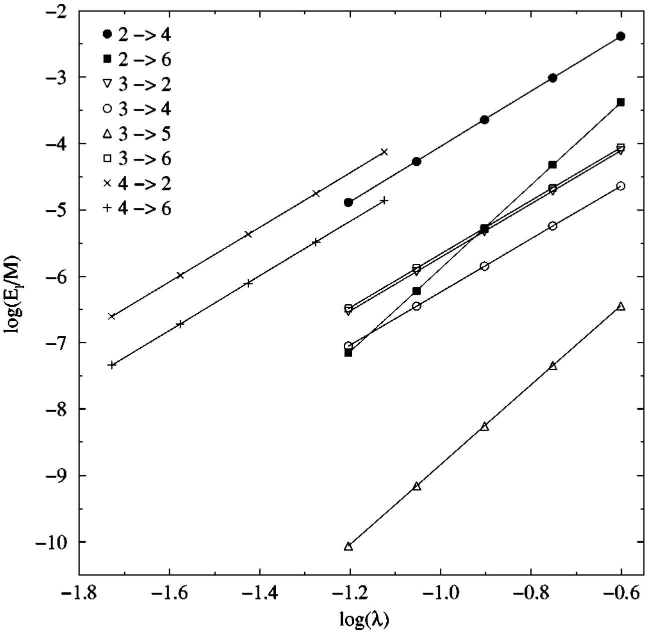

FIG. 9. Energy emitted in secondary harmonics as a fraction of the black hole mass, versus the amplitude of the initial data. The straight lines are linear best fits; the slopes and intercepts are given in Table II. All data points fit well to power laws, reflecting polynomial underlying couplings. The amplitude range of the $l=4$ family terminates at a lower value than the $l=2,3$ families because of higher sensitivity to caustic formation. One of the most remarkable facts uncovered in this nonlinear coupling analysis is that apparently the down scattering of $l=4$ to $l=2$ is the most efficient process among those studied.

TABLE II. Derived coupling exponents and coupling strengths based on the data of Table I. Eight couplings are studied in total, listed with a compact notation in the left column. Six couplings are seen to be quadratic, the other two being cubic (the energy scales as the square of the amplitude). The coupling strengths range in value. The most efficient quadratic process (at unit amplitude this would be the dominant quadratic process) transfers energy from the octupole harmonic to the quadrupole one. Near unit amplitudes, the cubic up scatterings appear to dominate generally. It is highly likely though that the examination of an $l=6$ primary evolution would reveal even more efficient cubic down scatterings.

| Coupling $ll'$ | Exponent $s_{ll'}$ | Strength $\epsilon_{ll'}$ |
|---|---|---|
| 24 | 4.2 | 1.3 |
| 26 | 6.3 | 2.5 |
| 32 | 4.0 | $2.0\times10^{-2}$ |
| 34 | 4.0 | $5.5\times10^{-3}$ |
| 35 | 6.0 | $1.5\times10^{-3}$ |
| 36 | 4.0 | $2.3\times10^{-2}$ |
| 42 | 4.1 | 3.1 |
| 46 | 4.1 | 2.1 |

eral important points about the coupling coefficients: The strongest coupling is a down scattering, namely, the 4→2 coupling. This means, in particular, that for an equal amplitude input, there is more nonlinear energy loss from an octupole to a quadrupole than the reverse, by a factor of more than 2. There is near parity between the 3→2 and 3→6 couplings, i.e., the nonlinear energy drain from the momentum-carrying $l=3$ mode is almost equally split between the zero-momentum $l=2$ and 6 modes.

## IV. SUMMARY AND DISCUSSION

A computational framework for the study of finite amplitude black hole perturbations has been developed on the basis of the characteristic initial value problem for the Einstein equations in an ingoing light-cone setup. A stable code with controllable resolution requirements was configured for delivering better than 1% signal accuracy for angular structures up to $l=6$. Finite amplitude perturbations were studied for total radiative energies up to 10% of the black hole mass. The examination of the distribution of energy in nonlinearly generated radiative modes provides some new insights into the dynamics of strongly perturbed black holes.

The main conclusions are that (i) the energy transferred through various couplings is found to obey simple power law scalings, up to the amplitudes studied. (ii) the nonlinear couplings are inefficient in channeling energy away from the primary mode, (iii) up scattering in $l$ space (the tendency to form ripples in the geometry) and down scattering (the tendency to smooth the geometry) are found to have comparable coupling strengths, with the distinct possibility that nonlinear smoothing is actually dominant, and (iv) various nonlinear effects are present during roughly the first $30M$ of evolution, including relative time delays of the different harmonics, phase reversals, and strong frequency evolution of oscillations before they reach their asymptotic value. The early periods are always smaller than the final QNM value, compatible with a picture in which the initial black hole is smaller. We note that the final values are found to agree well with those predicted by even-parity (polar) perturbations of Schwarzschild black holes [1]. Those are the black hole perturbations consistent with our symmetry assumptions and conditions (i.e., axisymmetry without rotation).

A relevant question is whether one can reasonably extrapolate to an arbitrary amplitude regime. The studies of black hole head-on collisions are probing a different, possibly stronger, regime of distortions (a proper assessment would require a study of invariants of the horizon geometry). It seems that the phenomenology of the response in such simulations is compatible with the picture laid out here. That is, collisions are genuinely nonlinear evolutions, which fail to generate visibly nonlinear signals because of inefficient off-diagonal couplings. The fairly independent evolution of individual harmonic modes, *a true nonlinear property of the Einstein equations as applied to the black hole system*, clarifies the larger than expected domain of applicability of infinitesimal black hole perturbations to collisions.

One can sharpen the picture by discussing a hypothetical nonlinear black hole regime that, apparently, does not happen. Motivated by other nonlinear hyperbolic systems, one could be excused for imagining an efficient and unrestrained energy cascade toward large $l$. The geometry of a sufficiently strong initial quadrupole perturbation could, say, ‘‘pinch’’ along certain angles, in a region visible to the exterior, hence emitting large amounts of energy in higher frequencies. This does not happen. Up scattering couplings, in addition to failing to dent the energy carried by the primary mode, seem to be also kept in check by the slightly more efficient down scattering processes. The conjecture is that this ‘‘diagonally dominant’’ nonlinear transfer matrix, with its appropriately tuned weights above and below the diagonal, is ultimately responsible for enforcing the nonlinear stability of a black hole to arbitrary distortions.

## ACKNOWLEDGMENTS

The author acknowledges support from the European Union program ‘‘Improving the Human Research Potential and the Socio-Economic Base,’’ via the network ‘‘Sources of Gravitational Radiation’’ (HPRN-CT-2000-00137) and the Nuffield Foundation (NAL/00405/G). He thanks J. Vickers and N. Anderson for discussions. Computations were performed on a Compaq XP1000 workstation at the University of Portsmouth.

[1] S. Chandrasekhar, *The Mathematical Theory of Black Holes* (Oxford University Press, Oxford, 1982).
[2] Binary Black Hole Grand Challenge Alliance, A. Abrahams *et al.*, Phys. Rev. Lett. **80**, 1812 (1998).
[3] L. Smarr, in *Sources of Gravitational Radiation*, edited by L. Smarr (Cambridge University Press, Cambridge, England, 1979).
[4] A. Abrahams, D. Bernstein, D. Hobill, E. Seidel, and L. Smarr, Phys. Rev. D **45**, 3544 (1992).
[5] P. Anninos, D. Hobill, E. Seidel, L. Smarr, and W-M. Suen Phys. Rev. Lett. **71**, 2851 (1993).
[6] D. Bernstein, D. Hobill, E. Seidel, and L. Smarr, Phys. Rev. D **50**, 3760 (1994).
[7] R.H. Price, Phys. Rev. D **5**, 2419 (1972).
[8] R.H. Price and J. Pullin, Phys. Rev. Lett. **72**, 3297 (1994).
[9] R. Gleiser, C. Nicasio, R.H. Price, and J. Pullin, Phys. Rev. Lett. **77**, 4483 (1996).
[10] S. Brandt and E. Seidel, Phys. Rev. D **52**, 870 (1995).
[11] K. Camarda and E. Seidel, Phys. Rev. D **59**, 064019 (1999).
[12] S.W. Hawking and G.F.R. Ellis, *The Large Scalar Structure of Space-time* (Cambridge University Press, Cambridge, England, 1973).
[13] M. van der Burg, H. Bondi, and A. Metzner, Proc. R. Soc. London **A269**, 21 (1962).
[14] R.K. Sachs, Proc. R. Soc. London **A270**, 103 (1962).
[15] L.A. Tamburino and J.H. Winicour, Phys. Rev. **150**, 1039 (1966).
[16] R. d’Inverno and J. Smallwood, Phys. Rev. D **22**, 1233 (1980).
[17] R. Bartnick, Class. Quantum Grav. **14**, 2185 (1997).
[18] C. Gundlach, R. Price, and J. Pullin, Phys. Rev. D **49**, 890 (1994).
[19] R.S. Hamade and J.M. Stewart, Class. Quantum Grav. **13**, 497 (1996).
[20] P. Papadopoulos and J.A. Font, Phys. Rev. D **63**, 044016 (2001).
[21] J. Winicour, Living Rev. Relativ. **4**, 2001-3 (2001).
[22] R. Gómez, P.L. Marsa, and J. Winicour, Phys. Rev. D **56**, 6310 (1997).
[23] R. Gómez *et al.*, Phys. Rev. Lett. **80**, 3915 (1998).
[24] R. Gómez, P. Papadopoulos, and J. Winicour, J. Math. Phys. **35**, 4184 (1994).
[25] R. Isaacson, J. Welling, and J. Winicour, J. Math. Phys. **24**, 1824 (1983).
[26] R. Penrose and W. Rindler, *Spinors and Space-Time* (Cambridge University Press, Cambridge, England, 1984), Vols. 1 and 2.
[27] P. Papadopoulos, E. Seidel, and L. Wild, Phys. Rev. D **58**, 084002 (1998).
[28] W. Krivan, P. Laguna, P. Papadopoulos, and N. Andersson, Phys. Rev. D **56**, 3395 (1997).